Vietnam Journal of Earth Sciences, 47(2), 290–314, https://doi.org/10.15625/2615-9783/23027

Vietnam Journal of Earth Sciences
https://vjs.ac.vn/index.php/jse

Advancing debris flow detection based on deep learning model and high-resolution images

Ngo Van Liem[1], Nguyen Hieu[1*], Dang Kinh Bac[1], Giang Tuan Linh[1,2], Dang Van Bao[1], Do Trung Hieu[1], Nguyen Minh Hieu[1], Dang Nguyen Vu[1], Dao Minh Duc[3]

[1]*VNU University of Science, Vietnam National University, Hanoi, Vietnam*
[2]*VNU Institute of Vietnamese Studies and Development Science (VNU-IVIDES), Vietnam National University, Hanoi, Vietnam*
[3]*Institute of Earth Sciences, Vietnam Academy of Science and Technology, Hanoi, Vietnam*

Received 09 January 2025; Received in revised form 23 May 2025; Accepted 10 June 2025

ABSTRACT

Debris flow inventory is an essential task for scientists and managers to mitigate danger to humans, especially in mountainous areas. However, rapid land use and cover change, as well as technological limitations, make it a challenging task. Monitoring debris-flow efforts, especially in hilly places with limited transportation and technology, may improve management to minimize damage caused by this hazard. This work assesses U-shaped deep learning architectures, focusing on the roles of image size, optimization procedures, and data quality in debris flow trace identification using U-Net and U2-Net. While new debris flows can be detected through machine learning modeling, the U-Net model, combined with the Adam optimizer and an input size of 64×64, has been proven to be efficient, accurate, and stable. Small debris traces that can be used for planning debris thickness maps were easily identified in Worldview-2 and UAV images but not in the medium-resolution remote sensing data. When applied to Bat Xat district, Vietnam, the models identified that the distribution of debris flows is not uniform and depends on natural factors, such as rainfall and human-interpolated factors, including the construction of structures. The study also establishes the need to continually assess and incorporate big data for enhanced debris flow hazard assessment and mitigation. Further developments should focus on the effective use of multi-spectral and large-scale topographic data to strengthen disaster risk identification and provide recommendations for disaster risk reduction.

Keywords: Deep learning; U-Net; U2-Net; debris flows; Vietnam.

1. Introduction

The global loss of life, property, and environment due to the impacts of debris flows has increased in recent years (Kean et al., 2013; Iverson et al., 2015). Cutting down trees, developing towns, severe rain, earthquakes, and volcanic eruptions transport soil, rock, and rubbish swiftly on hill slopes (Sánchez-Núñez et al., 2015). According to the WHO, landslides and debris flows killed 18,000 and injured 4.8 million between 1998 and 2017 (Carrión-Mero et al., 2021). Understanding how frequently and where debris flows occur can reduce the damage caused by this hazard to humans and the environment (Borrelli et al., 2014). However, global debris-flow monitoring requires extensive data collection and the selection of suitable indicators. Several approaches are employed to investigate the consequences of debris flow (Ren, 2015). Tectonic plates,

*Corresponding author, Email: nguyenhieu@hus.edu.vn

GPS, and inclinometers can detect and record debris flows in real-time, but only at a small scale in a particular location (Jason W. Satellite and aerial photos may reveal debris flow-prone regions changing in a larger scale (Kean et al., 2013; Su et al., 2024). These monitoring networks enable the government and experts to assess debris flow risk and alert the public immediately.

Commonly, field survey teams gather debris flow tracks, geography, and hazard monitoring along roads and residentials (Jiang et al., 2024). These ground-based investigations can reveal the size, speed, and initiation methods of debris flows, thereby improving remote sensing samples (H. Yang et al., 2024; Kuschel et al., 2024). Groups and professionals receive global debris flow data to identify patterns, trends, and causes of debris flow. Policymakers, managers, and first responders utilize these statistics to strengthen communities and reduce debris flow risk. Although monitoring and research have increased, the global numbers of debris flows remain challenging to inventory due to underreporting, errors, and usability issues following the rainy season (J. Zhang et al., 2024; Zhou et al., 2025). Therefore, scientists, managers, and international entities require an additional method to monitor and exchange debris flows.

There are various visual and analytical methods for detecting the shapes of debris flow traces in remote sensing images (S. Yang et al., 2024). They can be scars or shifting topography, distinctive morphological characteristics such as head scarps and debris fields, and altered plant patterns that can indicate the appearance of debris flow (Keller et al., 2015; Sánchez-Núñez et al., 2015). Casagli et al. (2023) suggested examining tone, texture, shadows, and lighting to identify debris flow sites. Images taken at various dates can be compared for temporal analysis to learn how landscapes change over time and identify rapid changes or movements associated with debris flows. These indications, combined with sophisticated image processing, help researchers discover and interpret debris flow paths in remote-sensing images. It lets individuals monitor debris flows and assess their risk (Varma Byrraju, 2019). Therefore, scientists and managers need a comprehensive indicator system that can discover collapse traces in field and satellite data.

Due to the constant change and complex shape of debris flows, selecting a suitable technology to identify, map, and characterize them is a challenging task (Pierson, 2005; Lee et al., 2024). Deep learning is one of the most developed technologies today in automatic object identification, serving the interests of protecting resources and the environment (Tran Anh et al., 2024; Nguyen Cong et al., 2024; Yasir et al., 2024b, 2024a; Nguyen et al., 2025; Nguyen Thanh et al., 2025). Recently, This technology can rapidly and reliably analyze collapse traces (Jiang et al., 2024; S. Yang et al., 2024). For example, CNNs and U-shaped structures automatically classify and detect debris flows in satellite images (Dang et al., 2022, 2024a). CNNs employ massive quantities of labeled data to identify complicated debris flow patterns and linkages and distinguish debris flows from other shapes and forms (Ghorbanzadeh et al., 2022). Previous studies employed Sentinel-1 and Sentinel-2 data to identify landslides using neural network models (Dang et al., 2024c). Deep learning algorithms aggregate data, extract characteristics, and simulate debris flows regionally. Additionally, computer scientists, geoscientists, and remote sensing experts must collaborate to improve algorithms, techniques, and technologies for utilizing remote sensing data in debris flow knowledge (Zhang et al., 2023; L. Zhang et al., 2024; Li et al., 2024). Thus, the potential of deep learning for debris flow trace detection enables the discovery and mitigation of dangers in rapidly changing environments today.

The study aims to propose a comprehensive indicator system and deep learning (DL) models for locating debris flow traces in WorldView-2 satellite images. Section 2.1.1 describes how the indicator system uses extremely high-resolution remote sensing and field observations. Section 2.2 discusses using DL models with various features in WorldView-2 images to locate debris flows. After that, our final DL models and signaling system are extensively tested throughout a particular region in the northern part of Vietnam. By employing multi-sensor remote sensing data to locate debris flows, this research demonstrates their practicality in real-world applications.

2. Material and methods

2.1. Debris flow detection deep-learning workflow

Figure 1 illustrates three ways to identify a debris flow trace. The extensive assessment in Section 2.1.1 identified debris flow indicators. On-site and lab tests were done. Debris flow trace samples were made at ground truth points (GTP) and from multi-temporal Worldview-2 images. Section 2.1.2 explains two types of U-shaped models from different sources. Deep learning methods, utilizing both conventional and cutting-edge architectures, teach computers to recognize debris flow traces on varied inputs in the second stage. Training models were rigorously evaluated in the third step. The models were tested using Worldview-2 images to prevent overfitting and underfitting. Phase 2 was developed and extensively tested based on new data to assess the model's performance and its potential in real-world applications. Lastly, researchers developed regional debris flow trace maps in particular regions.

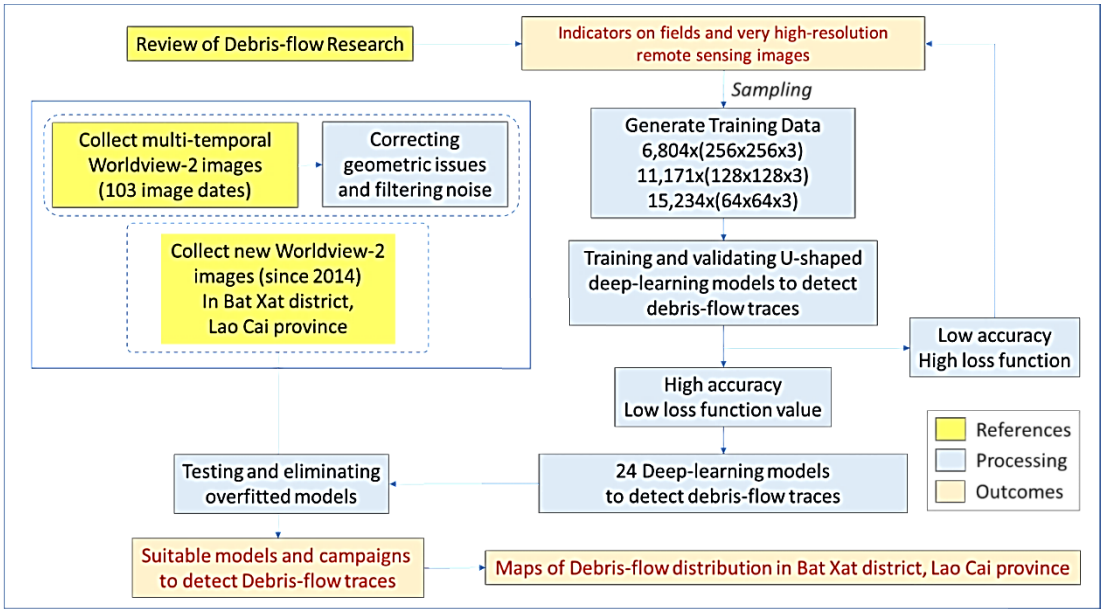

Figure 1. Deep-learning model construction procedure for debris-flow trace detection

2.1.1. Remote sensing and field debris flow indicators

Land-use planners and regulators need detailed inventories of debris flows, including topography, velocities, magnitudes, and substrates, to understand and develop suitable plans for minimizing their impacts (Yousefi et al., 2025). Nowadays, debris flow-prone locations can be identified and assessed using satellite and field images aided by trace

indicators (J. Zhang et al., 2024). Some indicators on fields include tension fractures, topography, plant patterns, and disturbed soil and rock (Fig. 2). These field indicators can reflect debris flow movements over time. Meanwhile, satellite images provide information on land cover, the spectral reflectance of different objects, and changes of terrain. Based on the very high resolution of some satellite sensors, optical images can monitor vegetation health and terrain changes.

Dao et al. (2008) clarified that debris flow is one of three particularly dangerous gravity landslides. This type of movement is also a form of landslide movement, characterized by a slide flow, where rainwater and groundwater play a direct and prominent role. Due to the thick, clay-rich weathering crust, the loose sediment layer on the surface is soaked with water when it rains for a long time. Debris flow behaves like a viscous mixture of rock and mud and then operates according to the sliding mechanism. Therefore, the destructive force is large, often causing fatal disasters. The indicators from field observations and satellite data, such as Worldview-2, shown in Fig. 2, enable the detection of debris flow traces and the identification of vulnerable areas for safety through monitoring, early detection, and informed decision-making.

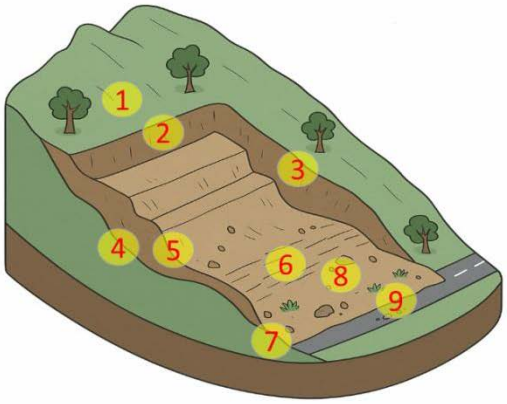

No.	Indicator	Field	RS Image
1	Summit Crown	X	X
2	Scarp	X	
3	Surrounding Flank	X	X
4	Slide Surface	X	
5	Main Body	X	X
6	Tension Cracks	X	
7	Concealed Surface	X	X
8	Overlying Foot	X	X
9	Downward Toe	X	X

Figure 2. Field and Worldview2-based debris flow indicators

Figure 2 shows comprehensive debris flow details from field and satellite images. Understanding debris flow dynamics requires knowledge related to the subject. Gallo and Lavé (2014) and Dang et al. (2024b) call the hill's leading edge the "Scarp" due to its high debris flow slope. The "Summit Crown" will remain until the next flow. Satellite and field images showed untouched debris on the "Surrounding Flank" of the flow. The "Slide Surface" is where material flows under the earth, and the "Main Body" is the debris block flow above the rupture surface. Field stress cracks indicate core ripping and fractures. Debris can be revealed on the "Concealed Surface," where green and grey surfaces meet. Additionally, the "Overlying Foot" and "Downward Toe" parts cover the pre-debris flow area and migrate downhill. Detailed debris flow indicators enhance our ability to monitor and assess geological phenomena, as well as identify debris flow traces in field observations and remote sensing data.

2.1.2. Data sampling

Samples were collected based on debris flow traces in Vietnam (Yellow regions in Fig. 3). Vietnam experienced 450 landslides, debris flows, and flash floods between 1953 and 2016 (Hung et al., 2015; Meinhardt et al., 2015). This statistic is questionable since not all debris flows were recorded. Based on

medium-resolution satellite images, scientists identified debris flows better. However, Dang et al. (2024a) proved that the use of this data can make small events disappear, leaving only big ones to be discovered. Accordingly, mountainous authorities systematically documented 8,500 locations of debris flows. In 5,000 locations, Pham et al. (2023) identified 61% of Northwestern landforms as debris flow-prone. These debris flows occur in complex, deeply cut mountainous terrain with abundant erosion and geological fragmentation. More than 2,700 small-scale debris flows have volumes higher than 100,000 m^3 (Vu and Nguyen, 2023). Based on these records, the authors arranged three field trips in six northeastern Vietnamese provinces between 2021 and 2023 to find debris flow traces. From July to September, debris flows damage provincial, district, community, and village roadways in these provinces. The recent increase in this hazard type has caused significant damage to roads, stations, electrical grids, hydrological systems, and water drainage networks, substantially halting traffic (Thao and Huong, 2022).

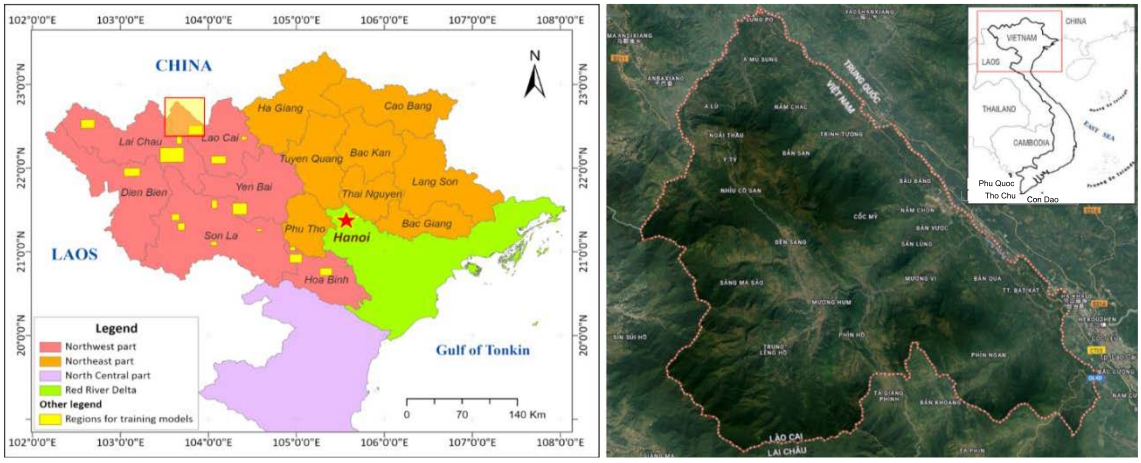

Figure 3. Field and remote debris flow trace sampling locations

Initial preparation collected the input sample in three steps. 0.7 m-resolution Google Earth Pro worldview-2 images vary in brightness. Therefore, a computer requires numerous data samples to classify debris flows. Google Earth Pro's samples in various years were maximized by saving photos as 5000 × 2500 *.JPG. The proper scale was 1:500. The application saved RGB pictures without background information. In six central Vietnamese provinces, including Yen Bai, Dien Bien, Lao Cai, Son La, Lai Chau, and Hoa Binh, multi-temporal samples were chosen. The use of images from different periods (2010–2023) introduces variability in lighting, vegetation phenology, and land-use change, thereby influencing the consistency of the debris flow training data. Attempts to address this included standardizing spatial resolution and image size as well as cross-referencing with field data to validate features across time. Debris flows have been observed in the selected areas for a decade (Fig. 2). Cross-referencing events with the remote sensing database found Worldview-2 images from 2014 to 2023. Accordingly, 2433 debris flows were digitalized from 103 image dates. Sampling spans 1,400 km^2 to collect debris flows of various sizes.

Step 2 was processed with all photo frames obtained from GEP software. Combining photos from the same year and area created full images (Fig. 3) to digitize traces of old debris flows. The high-resolution images of

GEP software contained spatial distortions; therefore, roads and other civil engineering works were used to correct them geometrically. This study altered geometrical aspects using ArcGIS Street-view data. Google Earth Pro three-dimensional models were utilized to analyze debris flow landforms visible from planted woodlands, and the border was manually digitized as a mask dataset in the second step.

High-resolution images show debris flows from peaks to debris flow toes. However, authors often struggle to identify debris flows in annual agricultural zones. Acacia and Eucalyptus dominate local reforestation. Acacia and Eucalyptus are harvested every 5–10 years in contemporary afforestation (Megown et al., 1999; Brockerhoff et al., 2013). After three to five years, farmers harvest Acacia and Eucalyptus. Agricultural planting or renewing changes land covers. Greenery became bare when plantation trees were taken down. Farmers dump timber from high altitudes onto open land for river transport. Harvesting activities created a debris flow-like topography at the forestry site (D'Amato et al., 2017). Land covers after deforestation mirror debris flow shapes (Fig. 4). Downstream accumulation sites may not follow the cut plantation wood boundary. Plantation forests change bare soil into young tree density in 2–3 years (Pham et al., 2024). False positives arise from these variations in forest cover that simulate debris flow forms. The study separated debris flow signatures from post-harvest plantation disturbances using extra land-use maps, vegetation indices (e.g., NDVI and BSI calculated from Sentinel-2 images), and deep learning model filtering rules to help mitigate this. New plantations and water flow zones may hide debris flow traces and slid vegetation. New growth may conceal these features, limiting the formation of new debris flows. Satellite image digitization of debris flow samples requires field changes for accuracy

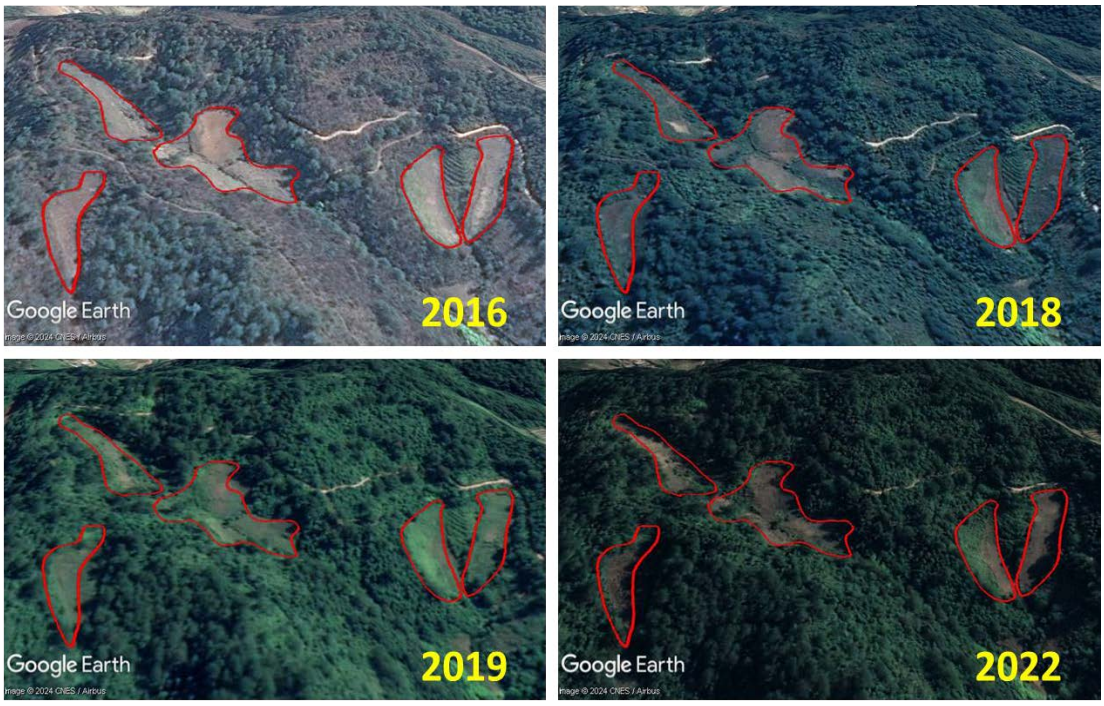

Figure 4. Traces of land use/cover changes look like a debris flow

On the field, the authors measured the size of debris flows and observed new traces. During three field excursions in Northwestern Vietnam from 2021 to 2024, the author verified and tested the application of debris flow indicators. Three fieldwork excursions were used to (1) find debris flow portions and compare them to Google Earth visual image interpretations, (2) measure and compute area and diameter, and (3) analyze land use/cover changes for digitization. After that, GGE images and mask data were made with "0" surrounding areas and "1" debris flow areas (Fig. 5). Worldview-2 data was "input images," whereas interpreted data was "input masks" in deep learning. Finally, large images were cut into sub-images. Six thousand eight hundred four sub-images were obtained if the input size was chosen as 256×256×3; 11,171 sub-images were obtained if the input size was selected as 128×128×3; and 15,234 sub-images were obtained if the input size was chosen as 64×64×3.

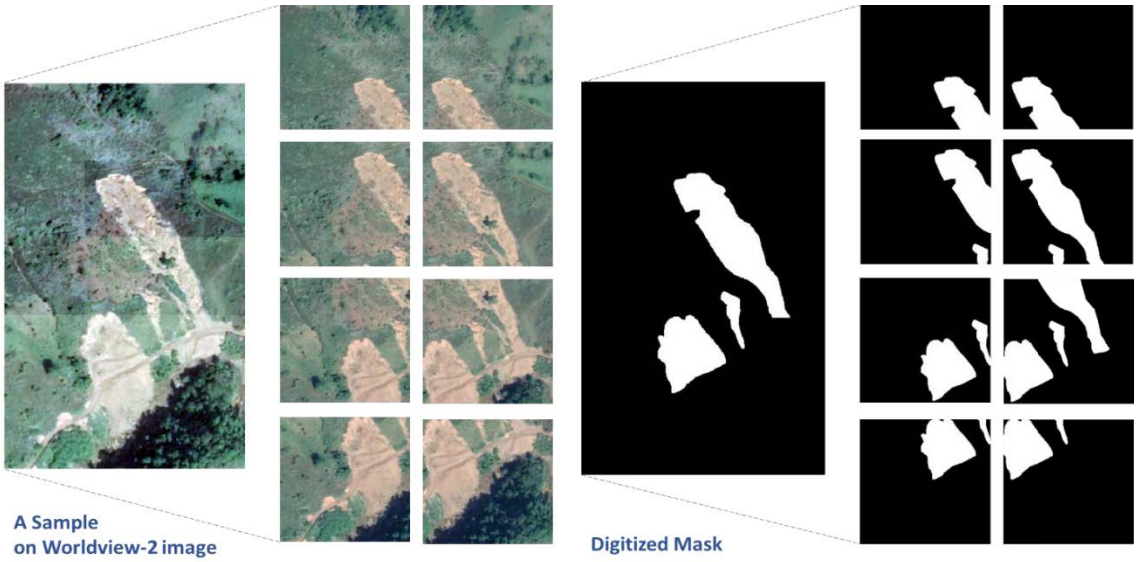

Figure 5. Cutting step to provide debris flow trace sample for DL model development

2.2. Selecting suitable deep-learning model architectures

2.2.1. Deep-learning architecture parts

Several new architectures, such as CNN, BiSeNet, and Dexinet, have been utilized to construct deep learning models. Some of the main parts that make up the structure of these architectures include input, convolution, Batch Normalization, Pooling, Concatenation, and Dropout layers (Sivapriya and Suresh, 2023; Tram et al., 2024). The training model evaluates all INPUT sub-images raw pixels before encoding. After processing, CONV filters may alter the input, and normalizing batches change data scales (Dong et al., 2022). The "Batch Normalization" layer reduces training "internal covariate shift" and loss of information in the training process (Wen et al., 2023). This layer modifies the standard deviation of the input layer through the following formula:

$$y_i = \alpha \widehat{x_i} + \beta \quad (1)$$

The parameters α and β are modified during training, whereas mini-batch $B(\{x_1 \ldots x_n\})$ mean and variance formulas determine α_i. POOL layers using activation techniques change the data to a 2×2 spatial matrix.

$$\delta_B \leftarrow \frac{1}{n}\sum_{i=1}^{n} x_i \quad (2)$$

$$\theta_B^2 = \frac{1}{n}\sum_{i=1}^{n}(\gamma_i - \delta_B)^2 \quad (3)$$

$$\widehat{y_i} \leftarrow \frac{p_i - \mu_B}{\sqrt{\theta_B^2 + \varepsilon}} \quad (4)$$

In the decoding process, "ConvTrans" layers are commonly used for upsampling matrices. Instead of training redundant neurons, DROPOUT layers locate and disable them (Diakogiannis et al., 2020). It prevents under- or over-fitting and generalization. Throughout the training, all deep learning models had layer input dropouts around 1.0. The number of above layers can be changed depending on the architecture of deep learning models. The allocation of each layer in the architecture also affects the model performance (Huang et al., 2020; Dong et al., 2022). Therefore, various state-of-art architectures have been developed and tested for different purposes. In this study, the authors selected two U-shaped architectures to optimize based on changes in the number and location of the above layers for detecting debris flow traces on high-resolution satellite images.

2.2.2. U-Net

Models based on the U-Net architecture (Fig. 6) have been used to analyze coastline changes (Giang et al., 2023) and land-use changes (Stoian et al., 2019). Its U-shaped design mimics the "U" and "U-Net" architectures, which include an encoder, bottleneck, decoder, Skip Connection, and output layers (Nava et al., 2022; Dang et al., 2024c). The U-shaped top plays a role in encoding or contracting data. Input image context and debris flow characteristics are extracted at the beginning. Pooling and convolutional layers lower input spatial dimensions and improve feature channels. In contracting, 3×3 convolutional layers filtered the data into multi-dimensional data layers. A bottleneck layer collects and stores the most abstract and crucial Worldview-2 image elements; such debris flow traces are at the bottom of the U-shaped structure (Stoian et al., 2019). This layer preserves geographic information while reducing the dimensionality of representation.

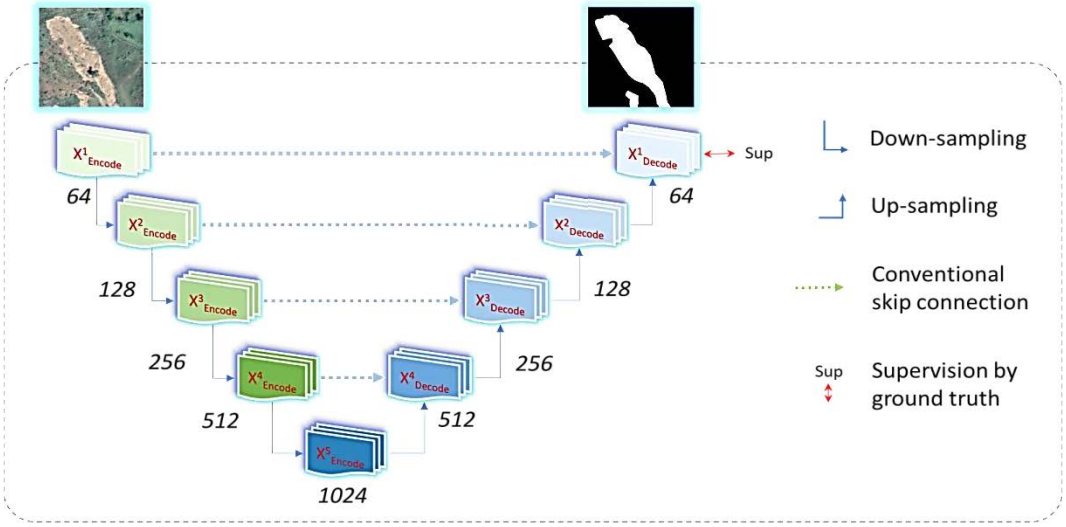

Figure 6. Debris-flow detection U-Net architecture using Worldview-2

After learning all the rules, the encoded data is enlarged. This novel filter count adjustment provides critical context and information for debris flow traces. Deconvolution or transposed convolutional layers enhance spatial resolution while

reducing the number of channels and modulating the number of filters from 64 to 1024 in the contracting route to restore the original information of data. Skipping connections preserve fine-grained and geographical features during upsampling (Boehm et al., n.d.). Afterwards, encoder-decoder data exchange is simplified. A 1×1 convolutional layer in the U-Net's final layer translates learned features to output channels. Results channels reflect the likelihood of debris flow or non-debris flow.

2.2.3. U2-Net

U2-Net design is developed based on U2-Net, a two-level U-structure architecture, to delve deeper, acquire high resolution, and reduce memory and processing costs (Qin et al., 2020). A single- or multi-level nested U-structure may have any positive integer exponent to make the network deeper. Instead of cascading stacking, the exponential notation of two implies a U-structure in each layer of a typical U-Net. Architectures with high levels are complicated to build and deploy. Limiting "n" exponential notation to two simplifies the concept (Fig. 7) (Dang et al., 2024c). U-Net stages include Residual U-blocks (Pouliot et al., 2019). A novel bottom ReSidual U-block harvests intra-stage multiple-scale features without reducing feature map resolution (Diakogiannis et al., 2020). The proposed U2-Net model encodes data at multiple scales with less processing and memory requirements than U-Net3+, as tested by Dang et al. (2024c). Accordingly, this architecture is simple enough to detect objects like debris flow traces. This architecture utilizes leftover U-Net components to operate in various scenarios with minimal performance loss.

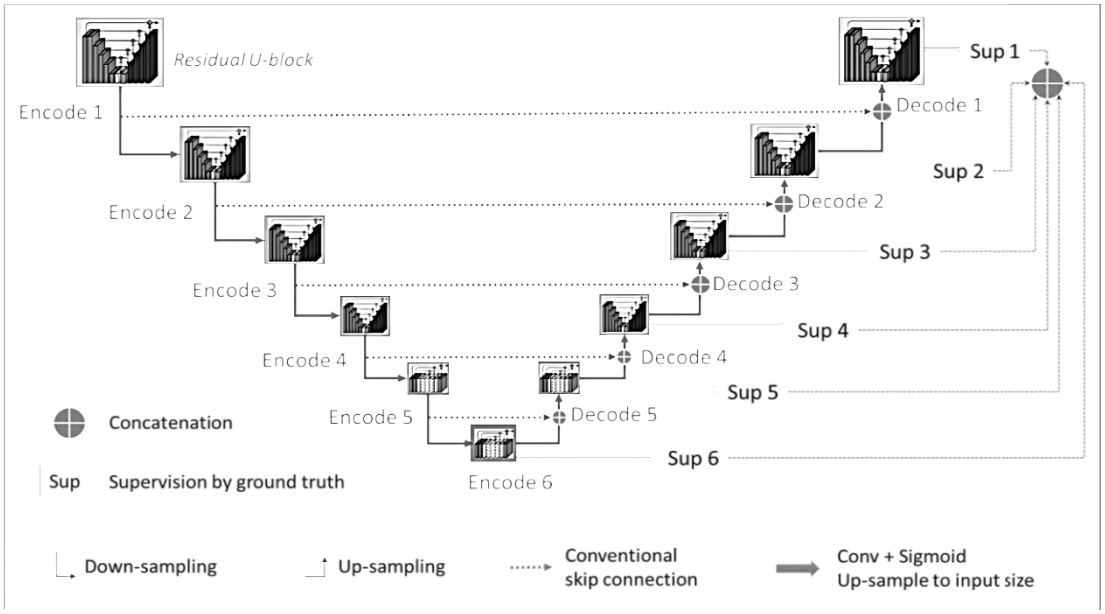

Figure 7. Debris-flow detection U2-Net architecture using Worldview-2

The architecture of the U2-Net used in this study contains six encoders, five decoders, and one fusion module before coming to the outcome layer. The first four encoder stages downsample input. To preserve context, the fifth and sixth encoder stages utilize dilated convolution to match the pixel resolution to the data. The decoder and encoder phases

match in the sixth encoder. Concatenating unsampled feature maps from the previous level and an asymmetrical encoder stage link to a responding decoder stage. The fusion module builds debris flow probability maps in the outcome layer. The U2-Net outputs six side debris flow probability maps using a sigmoid function and 33 Conv layers blended in stages En(6), De(5), De(4), De(3), De(2), and De(1). Concatenation, 1x1 convolution, and sigmoid function generate the final debris flow probability map in the last layers.

2.3. Optimization methods

Final deep learning models to predict debris flows must be developed without overfitting or underfitting. To verify the debris flow outcomes in the training and validation dataset, total accuracy (ACC) and loss function values were used.

2.3.1. Model evaluation techniques

Trained models are evaluated using six indices: "accuracy," "dice," "precision," "recall," "f1", and "loss function". First, accuracy is defined as the ratio of accurate predictions to the data samples utilized in the assessment (Liu et al., 2019). When data classes are expected to have equal sample sizes, this technique is used. In this study, 50% of samples were taken in identified debris flow traces, and 50% of samples were taken in the non-debris-flow areas. All input data were separated into training (70%) and validation (30%) sets. All evaluation indices were recorded during both the training and validation processes. Where "n" is the total number of sub-images; P is the predicted outcomes, and G is the ground truth samples; P_i is the predicted label for the i^{th} sub-image, and Q_i is the ground truth (actual) label for the i^{th} sub-image; $1(P_i = Q_i)$ is an indicator function that returns: 1 if $P_i=G_i$ (correct prediction) and zero if $P_i \neq G_i$ (incorrect prediction).

Firstly, the accuracy value is calculated as follows:

$$Accuracy = \frac{Number\ of\ true\ predictions}{Total\ number\ of\ input\ samples} = \frac{1}{n}\sum_{i=1}^{n} 1(P_i = Q_i) \quad (5)$$

Second, Dice coefficients are utilized to compare predicted and actual outcomes (Seale et al., 2022). The metric compares the intersection area of projected and actual outcomes to their total. A Dice score of around 1 indicates that the model correctly separated the data, as the expected and actual outcomes matched. The dice value formula is as follows:

$$Dice = \frac{2 * |P \cap G|}{|P| + |G|} \quad (6)$$

Thirdly, precision measures a model's ability to predict both positive and negative outcomes accurately. The statistic assesses the ratio of correctly anticipated negative to positive events. Due to its precision, the model seldom mis-predicts negative scenarios as positive. The calculation formula for precision value is presented as follows:

$$Precision = \frac{Number\ of\ true\ positive\ predictions}{Number\ of\ positive\ predictions} = \frac{\sum_{i=1}^{n} 1(P_i=1 \wedge G_i=1)}{\sum_{i=1}^{n} 1(P_i=1)} \quad (7)$$

The fourth metric of a model's performance to estimate all dataset positives is "recall" (Abdallah et al., 2020). The statistic measures the ratio of correct optimistic predictions to the total number of positive cases in the dataset. A high recall suggests that the model can identify positive instances but may mispredict negative ones. Recall value formula is presented as follows:

$$Recall = \frac{Number\ of\ true\ positive\ predictions}{Total\ number\ of\ positive\ samples} = \frac{\sum_{i=1}^{n} 1(P_i=1 \wedge G_i=1)}{\sum_{i=1}^{n} 1(G_i=1)} \quad (8)$$

As the fifth metric, the F1 Score assesses a deep learning model's performance in identifying all optimistic predictions while reducing false positives simultaneously (Ju et al., 2022). Therefore, this metric uses the harmonic average of Precision and Recall based on the following formula:

$$F1\ score = \frac{2 * (Precision * Recall)}{Precision + Recall} \quad (9)$$

Lastly, weight, image size, and label changes may cause a loss of data information during up- and down-sampling when calculating the F1 score. Models reduced loss function ($\mathcal{L}$) to reduce input data loss (Dang et al., 2020). Weight optimization lowers information loss and improves debris flow forecasts. Average loss for all training sub-image datasets:

$$\mathcal{L} = \frac{1}{n}\sum_{i=1}^{n} \ell^{(i)} \quad (10)$$

"n" represents training data, whereas $\ell^{(i)}$ Shows loss for "i" trained sub-image. All deep learning models used TensorFlow Keras API for training, validating, and testing (Studer and Falbel, 2019). Testing and validating accuracy were verified throughout the training process. Coefficient convergence halted deep learning training after 50 epochs.

2.3.2. Model precision optimization

Various deep-learning methodologies have been employed to enhance U-shaped models, such as modifications to the architecture, training size, and optimization algorithms. This section examines all possibilities to improve the accuracy of trained U-shaped models. Firstly, the input samples were configured with training sizes of 64×64, 128×128, and 256×256. Secondly, the number of filters in the Conv layers was changed from 8, 16, and 32 to 64. These changes can modify the size and characteristics of input training samples before the computer can learn.

Additionally, using the optimal optimization process is the most expedient approach to identifying a model that achieves superior accuracy and minimal loss function (Nhu et al., 2020). This study used the Adam, Adagrad, Adadelta, and SGD optimizers to identify the optimal weights for trained models (Table 1). During the optimization cycles, the evaluation functions of the trained models, as mentioned in Section 2.3.1, were computed continually. Following each epoch, the weights of all trained U-Net models were adjusted to reduce weight loss for the subsequent evaluation. This graphic encapsulates the previously examined optimization strategies. The training size and quantity of filters varied according to the optimizer method.

Table 1. The chosen methods to optimize parameter weights in trained U-shaped models to detect debris flow traces, adapted from Gulli and Pal (2017); Iglovikov et al. (2017); Wang et al. (2017); Alom et al., (2019); Falbel et al. (2019)

Formula	Model name	Optimizer	Algorithms
2	U-shaped-Adam	Adam	$w_{s+1} = w_s - \frac{\eta}{\sqrt{\hat{v}_s}+\epsilon}\hat{m}_s$
3	U-shaped-Adagrad	Adagrad	$w_{s+1} = w_s - \frac{\eta}{\sqrt{g_s+\epsilon}}g_s$
4	U-shaped-Adadelta	Adadelta	$\Delta w = -\frac{RMS[\Delta w]_{s-1}}{RMS[g]_s}g_s$; $w_{s+1} = w_s + \Delta w_s$
5	U-shaped-SGD	SGD	$w_{s+1} = w_s - \eta_s.\nabla_w Q\left(w_s; x^{(i)}; y^{(i)}\right)$
where w is parameter weight; η is the learning rates; t is step number; $\epsilon = 10^{-8}$; g_s is the gradient; m, v are values of first and second moments; η – step size			

2.4. Advanced Debris Flow Trace Interpretation

After selecting the most optimal model, it was used to examine debris-flow traces in new Worldview-2 images from 2010 to 2023 in Bat Xat district, Lao Cai province, Vietnam. Combining 1,542 small images obtained from the Google Earth Pro software yielded four large ones. This novel prediction algorithm requires no data preprocessing. The trained model converts image input into three-dimensional matrices. These data contain different sizes of the identified debris-flow traces. Fully Connected (FC) achieves slope avalanche limitations for detecting debris flows. The interpreted outcomes were compared to August 2023 and March 2024 field trips in ground control sites. Section 4 discusses how difficult debris flow classification is and how our findings compare to others.

3. Results

3.1. Performance analysis

Table 2 presents an overview of debris-flow detection models assessed via diverse setups and performance indicators. The design of the backbone and the quality of the data substantially affect the performance of the models. The computing configuration used for training significantly influenced modeling duration and file size. All nine models were trained on an HP Z800 workstation, equipped with a 12th Gen Intel(R) Core(TM) i7-12700KF CPU (3.60 GHz), 32 GB of RAM, and an NVIDIA GeForce RTX 3070 GPU. The simplified setups included two U-Net models, which required just one hour of training and yielded reduced file sizes of approximately 30 MB. Only training and validation datasets were used to calculate performance indicators. The stated high accuracy and low loss values imply strong performance; however, the optimum debris flow trace identification model must be established using independent testing datasets to prevent overfitting.

Although U2-Net may not always achieve the best accuracy or lowest loss, different versions of the network, such as models 13 and 21, are more successful than U-Net in terms of Dice and Recall, especially in identifying debris flows over a wide area. It appears that U-Net models perform well in marking out neat and concentrated traces, whereas U2-Net is better for detecting general regions of diffuse debris flows. For this reason, the outcome will determine which network is preferable: if accurate detection is key, U-Net is better, but U2-Net can provide broader coverage.

The training and evaluation procedures for the leading models disclose intriguing patterns. U-Net models have been regularly shown to enhance accuracy and stability across many setups. The U-Net model, with an input size of 64×64, achieved a peak accuracy of approximately 92.4% and demonstrated consistent validation loss metrics. Although the trained U-Net model with a 256×256 input size reached the highest accuracy (~96.6%) with a stable converging trend, the dice, precision, and F1 values of this model are lower than 75%. Meanwhile, the U-Net models using 64×64 input size remain these values higher than 83%.

In comparison, U2-Net models had more performance variability (Fig. 8). The 64×64 U2-Net model achieves an accuracy of 87.7% but exhibits varying Dice coefficients. Extended training periods and loss values showed that U2-Net models were more susceptible to optimization strategies because of their high processing needs.

Table 2. Performance Analysis of 24 Deep Learning Models for Debris Flow Detection

No.	Input size	Architecture	Optimizer	Loss function		Accu-racy	Dice	Precision	Recall	F1
				Training	Validating					
1	64	U-Net	Adam	0.23	0.17	92.4	83.7	85.8	86.3	86.1
2	64	U-Net	Adagrad	0.21	0.19	92.3	83.4	85.8	85.9	85.9
3	64	U-Net	Adadelta	0.32	0.18	92.4	83.9	85.3	87.1	86.2
4	64	U-Net	SGD	0.25	0.22	92.4	83.1	86.4	85.5	85.9
5	64	U2-Net	Adam	0.23	0.18	92.3	83.6	85.4	86.6	86.1
6	64	U2-Net	Adagrad	0.36	0.31	84.6	54.8	74.4	66.6	70.3
7	64	U2-Net	Adadelta	0.28	0.27	87.6	71.3	77.1	77.3	77.2
8	64	U2-Net	SGD	0.25	0.27	87.7	71.3	77.9	76.4	77.2
9	128	U-Net	Adam	0.13	0.12	94.5	76.4	79.1	80.1	79.5
10	128	U-Net	Adagrad	0.13	0.13	94.5	75.8	80.1	78.5	79.3
11	128	U-Net	Adadelta	0.14	0.13	93.9	74.7	79.8	79.2	79.7
12	128	U-Net	SGD	0.17	0.15	92.6	72.6	75.1	76.9	77.2
13	128	U2-Net	Adam	0.12	0.12	94.6	77.1	79.7	80.2	79.9
14	128	U2-Net	Adagrad	0.17	0.16	92.7	58.2	75.5	67.1	71.1
15	128	U2-Net	Adadelta	0.27	0.23	89.8	43.4	67.1	47.3	55.4
16	128	U2-Net	SGD	0.27	0.23	89.6	45.5	67.8	41.8	52.3
17	256	U-Net	Adam	0.02	0.01	96.6	66.6	78.5	72.7	75.2
18	256	U-Net	Adagrad	0.09	0.08	96.6	66.8	79.3	72.5	75.5
19	256	U-Net	Adadelta	0.08	0.05	95.8	64.6	77.4	71.6	73.2
20	256	U-Net	SGD	0.07	0.04	94.5	65.3	76.9	71.4	71.5
21	256	U2-Net	Adam	0.11	0.09	92.7	68.6	75.3	71.3	72.8
22	256	U2-Net	Adagrad	0.13	0.10	86.4	64.4	72.6	69.6	70.6
23	256	U2-Net	Adadelta	0.21	0.18	83.8	65.9	73.5	70.3	75.6
24	256	U2-Net	SGD	0.16	0.13	81.9	67.5	76.8	68.4	71.4

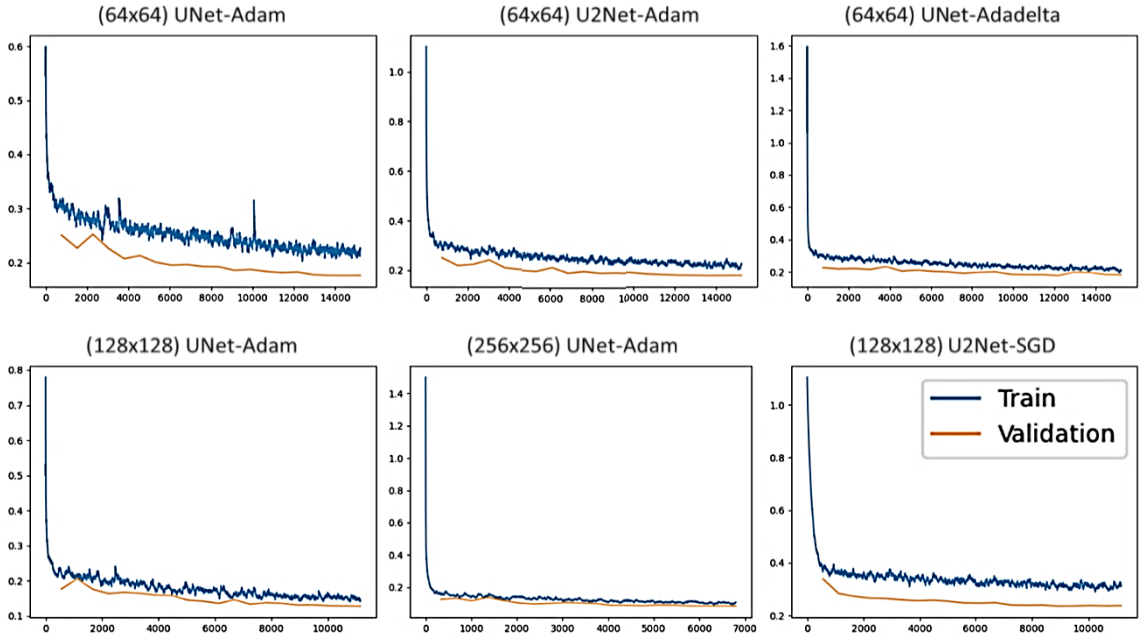

Figure 8. The performance of the model-development process of the best six deep-learning models for debris flow extraction is based on very high-resolution images

The model's actions are often determined a lot by the selected optimizer. Many networks that work well and converge quickly are created by adding adaptive rates and momentum to the Adam optimizer. Since it controls the learning rate, Adagrad functions effectively on sparse data; however, over time, this rate vanishes, and performance suffers. To address this, Adadelta adjusts the gradient development and allows the learning rate to change as needed. Because the balance of the learning rate is essential in SGD, the method is not always the best solution. In both U-Net and U2-Net topologies, the Adam optimizer consistently produced optimal results, striking a compromise between accuracy and loss reduction. The Adagrad and Adadelta optimizers were comparatively ineffective, especially for U2-Net models, often leading to elevated loss values and diminished stability in performance measurements.

3.2. Best U-shaped Model for Debris Flow Detection

Figure 9 illustrates the detection results of large debris flows using different U-shaped models with various training algorithms and input sizes, highlighting the diversity in detection ability and accuracy. For the U-Net (Adam) model, when the input size is 256×256, the results show that the marked areas are quite detailed but focus only on large slides, ignoring more minor details. When the input size is reduced to 128×128, the detection ability is significantly reduced, especially at the edges. At 64×64, the marked area becomes large, but accuracy is reduced dramatically, resulting in a significant amount of noise.

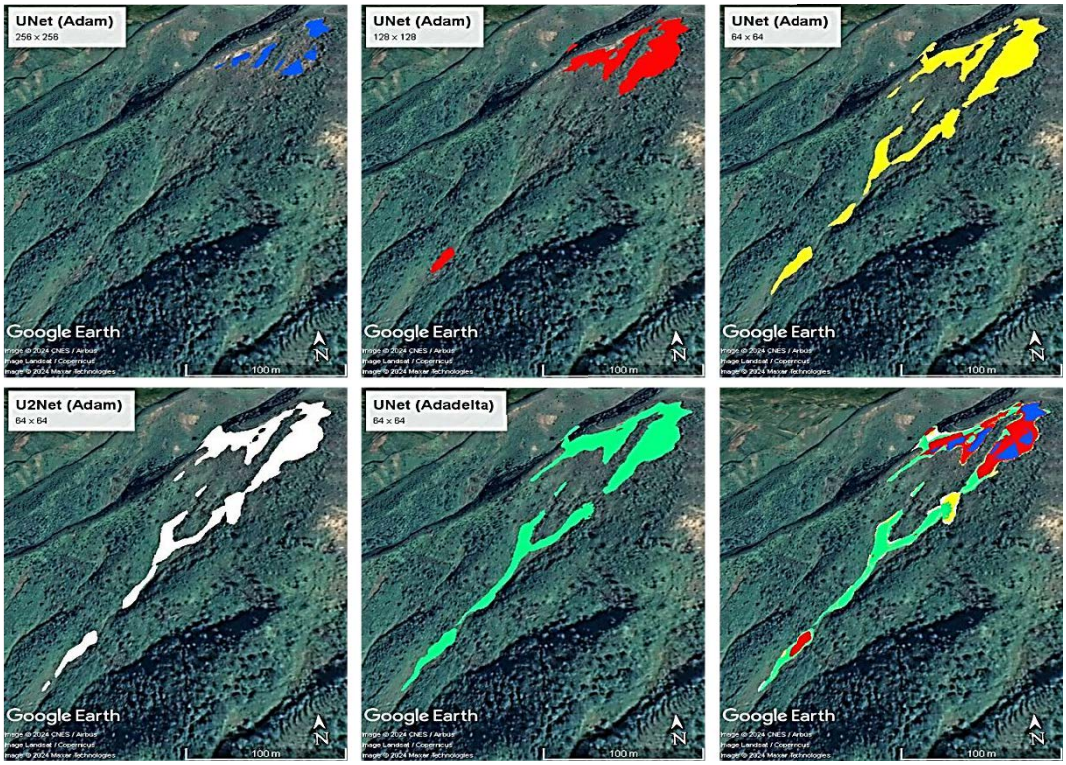

Figure 9. Outcome comparison of the U-shaped DL models in large debris flow trace detection on a slope. The color shows the different debris-flow regions detected from five DL models. The right bottom sub-figure shows the overlayed areas to see the more apparent differences

In such situations, U-Net proves helpful for outlining large debris flows where the image has high resolution; however, its performance suffers at smaller image sizes. The U2-Net (Adam) model detects huge areas, including non-slide traces. This suggests that, while it is sensitive to general features, it cannot fine-tune. The U-Net (Adadelta) model, with an input size of 64×64, is better at detecting large slip areas and has good coverage; however, noise still persists. The choice between U2-Net (Adam) at 64×64 and U-Net (Adam) at 128×128 or 256×256 should depend on whether you need to survey a wide or narrow area; the wider-area method is better for wide-area detection, but the finer-scaled one is for more accurate identification. The combined model results show that agreement between places found by more than one model is usually more accurate. However, it is still easy to see the differences between the methods. U-Net (Adam), which has a bigger input size, is better at finding large slips in detail. U2-Net (Adam) and U-Net (Adadelta), on the other hand, are better at covering large areas, but they need to be improved to lower noise and find a better balance between accuracy and detecting range.

Figure 10 shows what happens when different deep-learning models are used to find debris flows in a watershed. It demonstrates that the choices and methods were effective in various situations. First, the U-Net model, using the Adam optimization method and a 256×256 size, identifies a few collapse tracks. In other words, the high level of accuracy might not be suitable for modeling small, complex objects on the ground. Reducing the input size to 128×128 improves the model's ability to detect collapse tracks, and the results show more details in specific areas. Further decreasing the resolution to 64×64 with the Adam optimizer, the model detects more zones that are distributed across the basin. This indicates that this size is more suitable for studying complex landscape features.

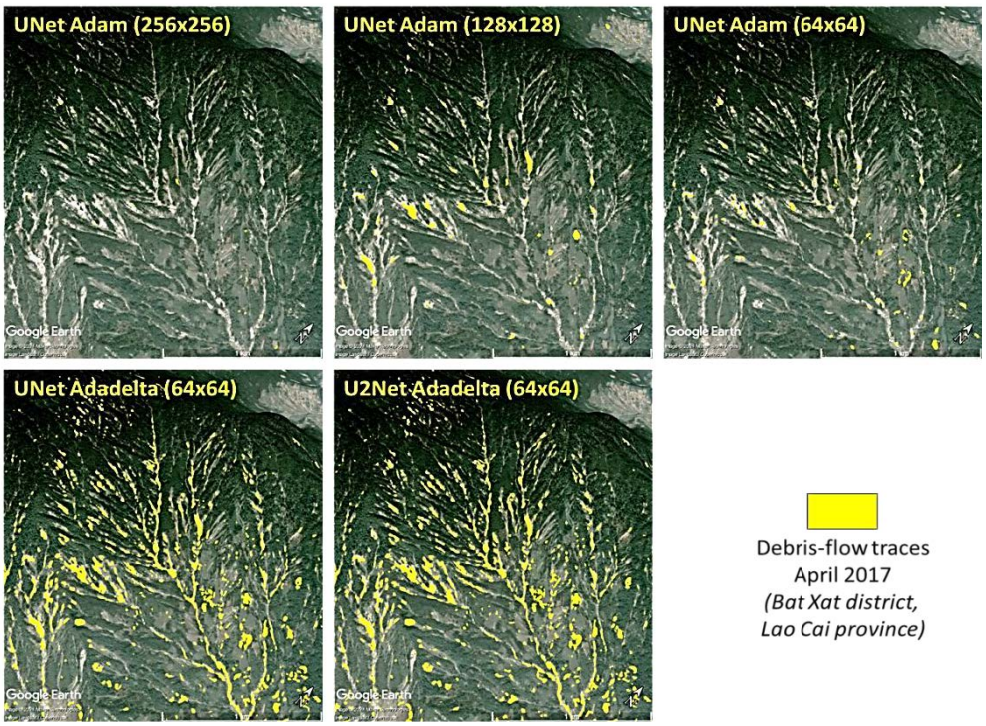

Figure 10. Outcome comparison of the U-shaped models in small to medium debris flow trace detection in a basin. The smaller input size allows for the detection of more debris flows

U-Net performs significantly better with the Adadelta optimization method at a 64×64 size, achieving both accuracy and clarity. The yellow regions indicate where debris flows occurred in 2018 and 2019 in the Bat Xat district. In this case, the Adadelta method shows that it made the model converge better than Adam. The U2-Net model with the Adadelta method and the same 64×64 scale merged both debris flows with regular flows containing rocks on the bottom. It illustrates the reality of the flows during heavy rain. All these regions were covered by water. However, after rainfall, debris flow traces can be observed in the yellow areas, as indicated by the U-Net Adam (64×64) model.

3.3. Debris flow Monitoring in Bat Xat district, Lao Cai province

The research used the U-Net-Adam model with an image dimension of 64×64, as indicated by the model comparison findings, to examine various regions, yielding the outcomes shown in Fig. 11. The pink dots on the map, indicating debris flow occurrences, reveal a very irregular distribution throughout various regions in Bat Xat district. Most of the debris flows are in the western part of the district, where there are five debris flows for every 10 ha. The southern part of the area also had major failures, though not as many as in the western part. In some places that are yellow and orange, there are between a middle and a high number of debris flows. The land's shape, the amount of water on the top, or the ease with which the rocks and dirt in the area sink could all be to blame.

On the other hand, most of the central and eastern parts of the district are covered in green. There are few or no debris flows in those areas (0.10 debris flows per 10 ha). These places have fewer steep slopes, more stable ground, or are less influenced by factors that can cause debris flows, such as heavy rain or human activities. The location of debris flows is also closely connected to both natural and human-made factors. Debris flow hotspots are often found near major roads or rivers, where the ground can be worn away by buildings, traffic, or water. This study helps identify high-risk areas, enabling more effective land management and disaster prevention.

The satellite images, spanning from 2013 to 2020, show how the debris flows changed over that period in the study area. The places that were damaged are shown in pink. Initially, on 14 June, 2013, the collapse affected only a small area and was spread out over several smaller areas. By 16 March 2015, the debris flows had significantly expanded, with more eroded strips, especially spreading near the hilly parts close to the road (Fig. 12). On 23 March 2017, the debris flows continued to increase in size, with the pink areas spreading, showing the increasingly apparent impact on the entire hilly landscape. By 6 February 2019, the debris flow was at its most intense, with large slide strips appearing and developing deeper into the hilly area. On 18 April 2019, the debris flow continued to expand, although its speed seemed to have slowed compared to the previous period; however, the affected areas became more clearly defined. The debris-flow area tended to stabilize, although erosion at the margins persisted, and the expansion slowed down by 18 December 2019. Ultimately, the debris flow attained its zenith on 10 November 2020, as the debris-flow areas merged into larger regions. However, there was no significant expansion in comparison to 2019. The flow's gradual yet intricate growth, exemplified by substantial surges in 2015 and 2019, may be attributed to natural factors such as intense rainfall, fragile geological formations, or artificial influences like deforestation and construction activity, as illustrated in this sequence.

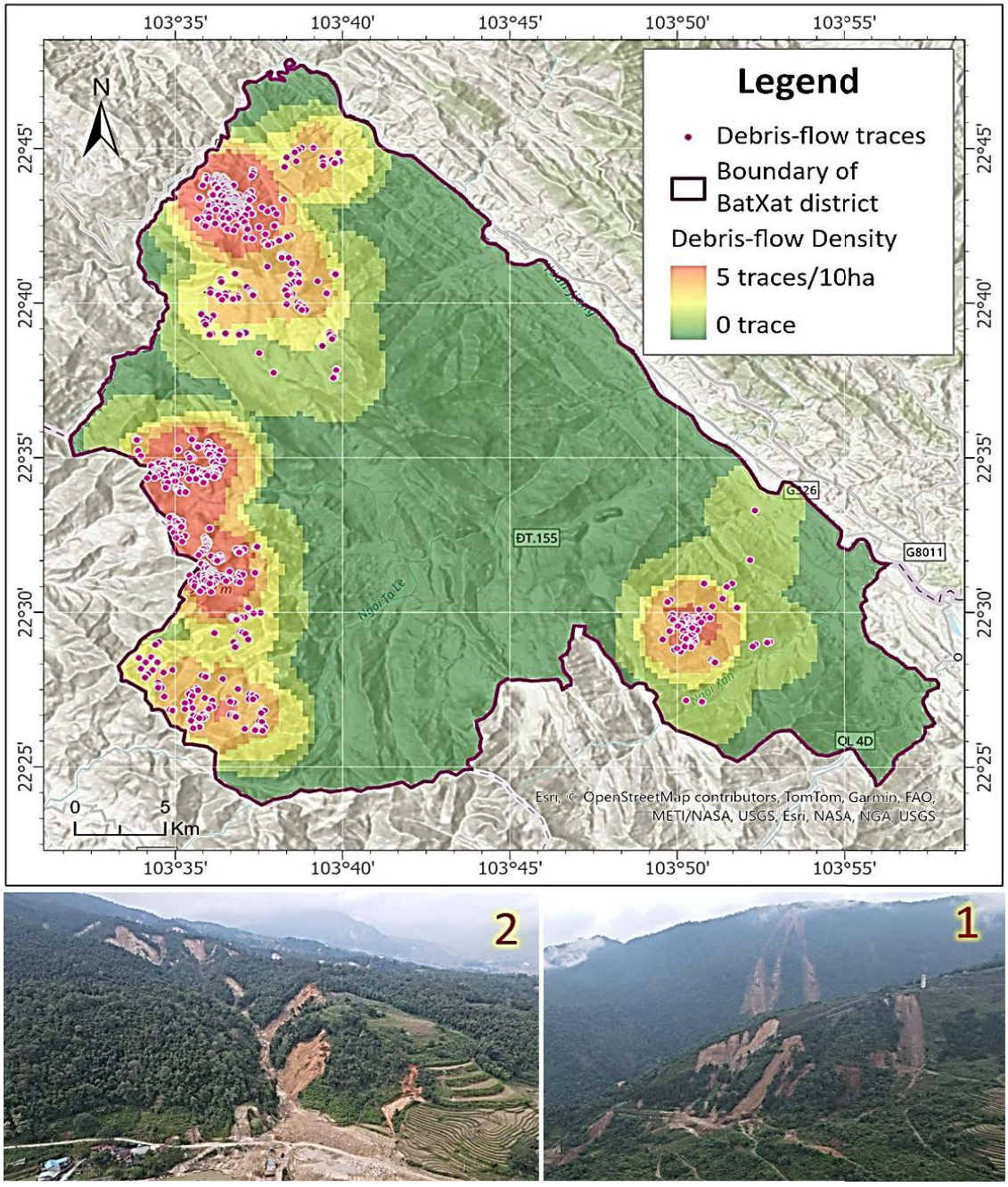

Figure 11. The appearance of debris flow traces after the rainy season in 2018 in Bat Xat district, Lao Cai province, Vietnam, was detected by a (64×64) U-Net-Adam model. The picture in the third region is shown in Fig. 12

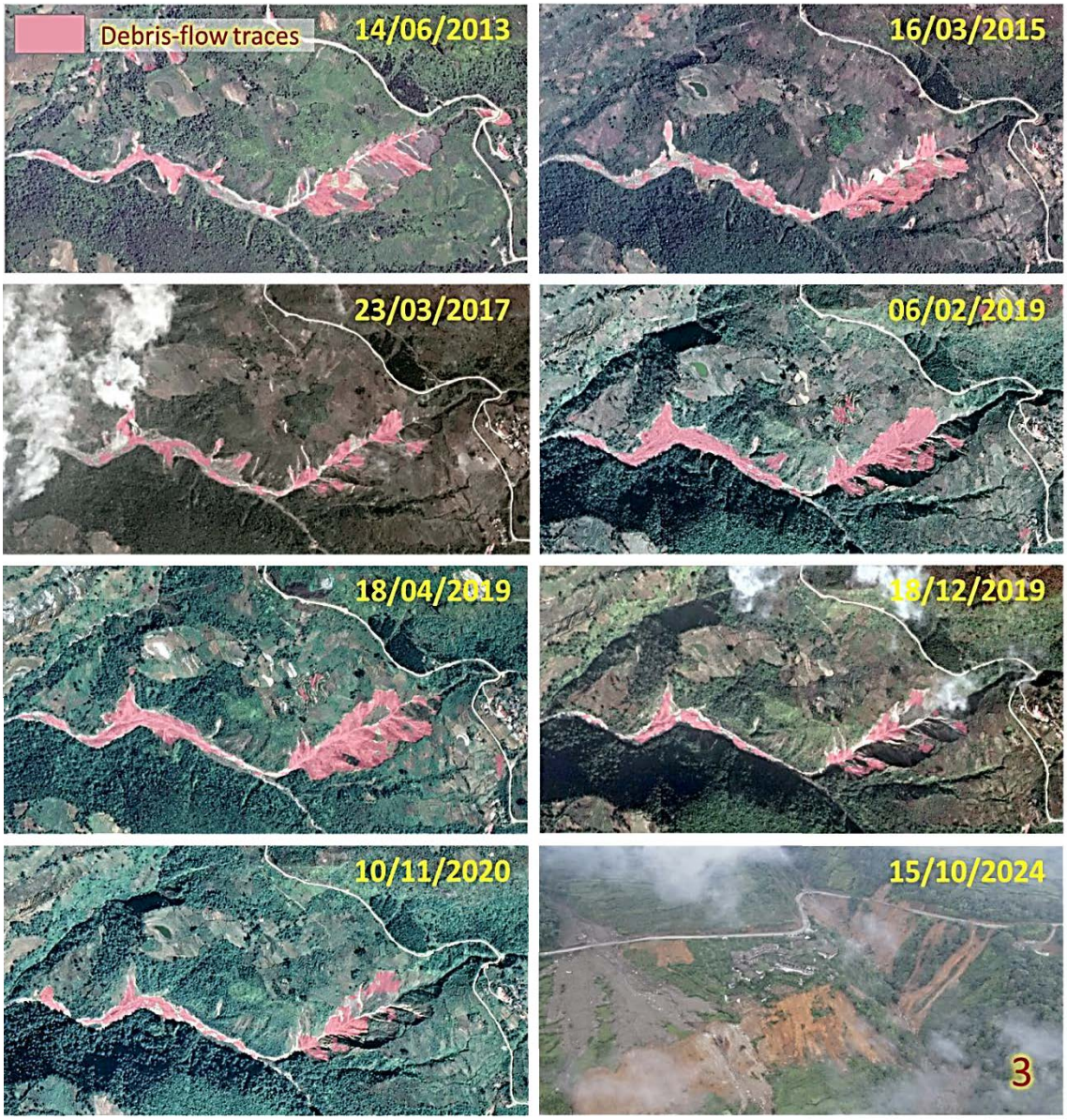

Figure 12. The evolution of debris-flow traces detected by the (256×256) U-Net-Adam model through satellite images (2013–2020) in the Y Ty, Bat Xat district, Lao Cai province (Region 3 in Fig. 11)

4. Discussions

4.1. Possible debris flow monitoring using remote sensing

Both U-shaped models can detect debris flow traces in three-band Worldview-2 images, especially in slope-unstable locations. Based on high-resolution images, as proposed by McKean and Roering (2004), Hung et al. (2015), and Kuschel et al. (2024), traces of natural hazards can be detected over data and technology constraints, even in limited areas. Compared to medium-resolution data (such as Landsat 8 and Sentinel-1 and -2), as done by Pour and Hashim (2017), high-resolution images helped DL models recognize small

debris flow traces. This study recommends using trained models to address the shortcomings of traditional mapping methods, which are complicated by the complex shapes of debris flows. Debris flows are often recurrent and inherited. It makes monitoring and assessing the movement and change of these hazards difficult if only visually and monitoring at specific location using traditional geological methods. The movement can be small, from 10-20m/year - equal to the spatial size of medium-resolution satellite images. Therefore, the high-resolution is needed to monitor the tiny movement of this hazard over time.

Kirschbaum et al. (2015) and Dang et al. (2024a) proposed that satellite images can be reviewed after annual disasters, allowing for the selection of suitable action and recovery solutions. Regarding spatial resolution, medium-resolution remote sensing data obscure the head, foot, and materials of debris flow traces larger than 1,200 m². Therefore, this data can only be used to identify debris flow locations rather than their borders. Based on the Worldview-2 images, this study enables scientists and managers, as demonstrated in the case study, to track debris flows and slope instabilities larger than 12 m², as previously done by Tran (2013) and Van Thang et al. (2021). Regarding the temporal resolution, Sentinel-1 can be obtained on average twice per month, while Sentinel-2 images can be obtained once per month, as done by Handwerger et al. (2021). Therefore, no weekly debris flow monitoring is feasible based on the medium-resolution data. Meanwhile, the high-resolution data may be obtained from Worldview-2, as well as UAVs. The trained models can detect debris flows in real time and update Vietnam's danger maps at any time.

Input data consistency plays a key role in the training and evaluation of deep learning models for detecting mudflows. In this study, remote sensing data were collected from various mountainous provinces in Northern Vietnam, primarily using high-resolution Google Earth Pro images (0.7 m) with a uniform scale of 1:500. However, spatial consistency still presents some challenges. These images were taken at various locations and times, resulting in differences in shooting angles, 3D terrain distortion, and geometric errors. Although calibration steps using roads and ArcGIS StreetView tools were performed, the risk of spatial errors still exists and can reduce accuracy when overlaying image samples from multiple areas. In addition, temporal consistency is also affected by the use of images from different years, spanning from 2014 to 2023. These remote sensing data are inconsistent in terms of seasonality, weather conditions, or time elapsed after the rock flow event. In particular, in areas with industrial plantations such as acacia and Eucalyptus, the 3–5 year planting-harvest cycles create large fluctuations in land cover, which can easily be confused with the actual rock flow traces. These changes reduce the reliability of images at different times without additional preprocessing steps such as NDVI analysis, land use mapping, or field validation. Therefore, maintaining spatial and temporal consistency is a prerequisite to ensure the representativeness and accuracy of deep learning models.

Monitoring and utilizing regional debris flow data is essential for creating big data and providing early warning signals. A comprehensive database of debris flow processes spanning months and years may help managers restrict development in debris flow-prone areas and adopt mitigation methods more quickly. Particularly in tropical countries, detecting, monitoring, and predicting debris flows requires high-resolution remote sensing due to the recent rapid changes in climate. Remote sensing images give statistical data and debris flow boundaries for classification and description. Training models can identify fractures, define events as active or inactive, calculate

movement speed, and monitor sliding blocks. They can become a powerful source of information for managers to provide suitable and timely decisions for upcoming natural hazards.

4.2. Deep Learning's Role in Debris Flow Monitoring in the Future

In this research, U-Net, rather than DeepLabv3+, Mask R-CNN, or Swin Transformer, as done by Ju et al. (2022), was chosen since it is simpler for a computer to process and performs well with less data. Since such advanced models require a significant amount of information, powerful computers, and a considerable amount of time to train, they are not well-suited for use in mountainous areas, where resources and conditions are limited. In contrast, U-Net enables fast training, a compact model size, and easy deployment and can achieve good performance with high-resolution but not overly diverse remote sensing data. Additionally, U-Net is more suitable for detecting traces of debris flows in mountainous areas where the terrain is rugged, and satellite images may be obscured by vegetation cover or haze. Therefore, using U-Net with optimal algorithms, such as Adam, is considered a reasonable choice, as it strikes a balance between accuracy, processing performance, and practical applicability.

The study indicated that U-Net, combined with the Adam optimizer, detects new debris flows more effectively than other options. In 24 trained models, four trained algorithms may discover debris flow traces. These findings suggest that the U-Net model may yield reliable results with an input size of 64 × 64. In addition to the accuracy metrics, the model's performance was evaluated using predictions for new data to prevent overfitting cases. The outcomes from the trained U-Net models outperformed those of other models in terms of segmentation accuracy, coming close to the ground-truth interpretation.

The optimization strategies and model development steps in this study can be used to develop new and more optimal debris-flow detection models in the future. The five accuracy values and loss functions monitor model performance during the training process, and different optimization methods were used to improve accuracy and efficiency. This optimizer creates reliable debris flow models when used in real-time monitoring. Managers and scientists may utilize trained deep-learning models to track debris flows following this research initially. However, this study's Worldview-2 image samples included 1,780 km^2 of debris flow and non-debris flow traces. More samples are needed for a functional monitoring system, especially with samples obtained from UAV data.

The authors tested the integration between Worldview-2 images and ALOS-DEM data at a 12.5 m resolution. However, it enables U-shaped models to differentiate between old and new debris flows. The U-shaped models were unable to capture a broad range of topographic features in the debris flow areas. It was found that topography changes are not representative of debris-flow and non-debris-flow regions, resulting in poor performance. As a solution, UAV-based debris flow monitoring should include both multi-spectral data and larger-scale topographical data. Remote sensing data and deep learning (DL) models developed in this study can be utilized for continuous, cost-effective debris flow monitoring in mountainous areas with limited resources.

5. Conclusions

Various U-shaped models were tested in this study, which demonstrates the importance of deep learning methods for debris flow detection. A field indicator system and high-resolution remote-sensing data are essential keys for locating debris flow traces. A careful investigation reveals that the input image size and backbone design have a significant impact

on model performance. The U-Net architecture, combined with the Adam optimizer method and a 64×64 input size, makes the system more optimal for identifying new debris flows outside the training data. It utilizes high-resolution remote sensing data to enhance debris flow monitoring and evaluation, allowing risk maps to be updated quickly.

Advanced tweaking and assessment of deep learning models used to forecast debris flows may enhance their accuracy and performance, particularly for debris flows in the Northwestern path of Vietnam. In resource-constrained environments, high-scale topographic data and continuous monitoring programs may improve model performance by leveraging big data collected over time. These findings help researchers, managers, and governments improve hazard risk prediction and reduce the damage from this hazard in the future.

Declaration of competing interest

The authors declare that they have no known competing financial interests or personal relationships that could have appeared to influence the work reported in this paper.

Acknowledgments

The paper was conducted under the national project funded by the Ministry of Science and Technology of Vietnam, code ĐTĐL.CN-41/23.

References

Abdallah A., Hamada M., Nurseitov D., 2020. Attention-Based Fully Gated CNN-BGRU for Russian Handwritten Text. Journal of Imaging, 6, 141. https://doi.org/10.3390/jimaging6120141.

Alom M.Z., Taha T.M., Yakopcic C., Westberg S., Sidike P., Nasrin M.S., Hasan M., Van Essen B.C., Awwal A.A.S., Asari V.K., 2019. A state-of-the-art survey on deep learning theory and architectures. Electronics (Switzerland), 8, 1–67. https://doi.org/10.3390/electronics8030292.

Boehm V., Ji Leong W., Bal Mahesh R., Prapas I., Kalaitzis F., Ganju S., Ramos-Pollan R., n.d. Deep Learning for Rapid Landslide Detection using Synthetic Aperture Radar (SAR) Datacubes. 1–8.

Borrelli L., Antronico L., Gullà G., Sorriso-Valvo G.M., 2014. Geology, geomorphology and dynamics of the 15 February 2010 Maierato landslide (Calabria, Italy). Geomorphology, 208, 50–73. https://doi.org/10.1016/j.geomorph.2013.11.015.

Brockerhoff E.G., Jactel H., Parrotta J.A., Ferraz S.F.B., 2013. Forest Ecology and Management Role of eucalypt and other planted forests in biodiversity conservation and the provision of biodiversity-related ecosystem services. Forest Ecology and Management, 301, 43–50. https://doi.org/10.1016/j.foreco.2012.09.018.

Carrión-Mero P., Montalván-Burbano N., Morante-Carballo F., Quesada-Román A., Apolo-Masache B., 2021. Worldwide research trends in landslide science. International Journal of Environmental Research and Public Health, 18. https://doi.org/10.3390/ijerph18189445.

Casagli N., Intrieri E., Tofani V., Gigli G., Raspini F., 2023. Landslide detection, monitoring and prediction with remote-sensing techniques. Nature Reviews Earth and Environment, 4, 51–64. https://doi.org/10.1038/s43017-022-00373-x.

D'Amato D., Rekola M., Wan M., Cai D., Toppinen A., 2017. Effects of industrial plantations on ecosystem services and livelihoods: Perspectives of rural communities in China. Land Use Policy, 63, 266–278. https://doi.org/10.1016/j.landusepol.2017.01.044.

Dang K.B., Dang V.B., Bui Q.T., Nguyen V.V., Pham T.P.N., Ngo V.L., 2020. A Convolutional Neural Network for Coastal Classification Based on ALOS and NOAA Satellite Data. IEEE Access, 8, 11824–11839. https://doi.org/10.1109/ACCESS.2020.2965231.

Dang K.B., Dang V.B., Ngo V.L., Vu K.C., Nguyen H., Nguyen D.A., Nguyen T.D.L., Pham T.P.N., Giang T.L., Nguyen H.D., Hieu Do T., 2022. Application of deep learning models to detect coastlines and shorelines. Journal of Environmental Management 320, 115732.

Dang K.B., Giang T.L., Dang V.B., Phan T.T., Truong Q.H., Ngo V.L., Do T.H., Dang N.V., Forino G., 2024a. Deep learning models integrating multi-

sensor and -temporal remote sensing to monitor landslide traces in Vietnam. International Journal of Disaster Risk Reduction, 105, 104391. https://doi.org/10.1016/j.ijdrr.2024.104391.

Dang K.B., Giang T.L., Dang V.B., Phan T.T., Truong Q.H., Ngo V.L., Do T.H., Dang N.V., Forino G., 2024b. Deep learning models integrating multi-sensor and -temporal remote sensing to monitor landslide traces in Vietnam. International Journal of Disaster Risk Reduction, 105, 104391. https://doi.org/10.1016/j.ijdrr.2024.104391.

Dang K.B., Nguyen C.Q., Tran Q.C., Nguyen H., Nguyen T.T.T.T., Nguyen D.A., Tran T.H., Bui P.T., Giang T.L., Lenh T.A., Ngo V.L., Yasir M., Nguyen T.T.T.T., Ngo H.H., Quan C., Cuong Q., Nguyen H., Thuy T., Hao H., 2024c. Comparison between U-shaped structural deep learning models to detect landslide traces. Science of the Total Environment, 912, 169113. https://doi.org/10.1016/j.scitotenv.2023.169113.

Dao D.B., Dang V.B., Nguyen H., 2008. Towards authentic warning of high-risk areas for some common natural disasters in Vietnam. Proceedings of the Third International Conference on Vietnam Studies. Hanoi National University Publishing House, 441–461.

Diakogiannis F.I., Waldner F., Caccetta P., Wu C., 2020. ResUNet-a: A deep learning framework for semantic segmentation of remotely sensed data. ISPRS Journal of Photogrammetry and Remote Sensing, 162, 94–114. https://doi.org/10.1016/j.isprsjprs.2020.01.013.

Dong Z., An S., Zhang J., Yu J., Li J., Xu D., 2022. L-Unet: A Landslide Extraction Model Using Multi-Scale Feature Fusion and Attention Mechanism. Remote Sensing, 14, 1–13. https://doi.org/10.3390/rs14112552.

Falbel D., Allaire J., François Tang, Y. Bijl, W. Van Der, Studer M., Keydana S., 2019. R Interface to "Keras."

Gallo F., Lavé J., 2014. Evolution of a large landslide in the High Himalaya of central Nepal during the last half-century. Geomorphology, 223, 20–32. https://doi.org/10.1016/j.geomorph.2014.06.021.

Ghorbanzadeh O., Shahabi H., Crivellari A., Homayouni S., Blaschke T., Ghamisi P., 2022. Landslide detection using deep learning and object-based image analysis. Landslides, 19, 929–939. https://doi.org/10.1007/s10346-021-01843-x.

Giang N.C., Chien N.Q., Khac D.V., 2024. Estimation of greenhouse gas emission due to open burning of rice straw using Sentinel data. Vietnam Journal of Earth Sciences, 46, 381–398.

Giang T.L., Dang K.B., Bui Q.T., 2023. Coastline and shoreline change assessment in sandy coasts based on machine learning models and high-resolution satellite images. Vietnam Journal of Earth Sciences, 45, 251–270.

Gulli A., Pal S., 2017. Deep Learning with Keras - Implement neural networks with Keras on Theano and TensorFlow. Packt Publishing Ltd., Birmingham, UK.

Handwerger A., Jones S., Amatya P., Kerner H., Kirschbaum D., Huang M.-H., 2021. Strategies for landslide detection using open-access synthetic aperture radar backscatter change in Google Earth Engine. Natural Hazards and Earth System Sciences Discussions, 1–35. https://doi.org/10.1016/j.jenvman.2022.115732.

Huang H., Lin L., Tong R., Hu H., Zhang Q., Iwamoto Y., Han X., Chen Y.W., Wu J., 2020. UNet 3+: A Full-Scale Connected UNet for Medical Image Segmentation. ICASSP, IEEE International Conference on Acoustics, Speech and Signal Processing - Proceedings 2020-May, 1055–1059. https://doi.org/10.1109/ICASSP40776.2020.9053405.

Hung P. Van, Son P.Q., Dung N. Van, 2015. The study evaluated arming of risk of lanslide in Hoa Binh and Son La reservoir hydropower area on the basis of analyzing high-resolution remote sensing and geographic information systems. Vietnam Journal of Earth Sciences, 37, 193–203.

Iglovikov V., Mushinskiy S., Osin V., 2017. Satellite Imagery Feature Detection using Deep Convolutional Neural Network: A Kaggle Competition. ArXivLabs - Computer Vision and Pattern Recognition.

Iverson R.M., George D.L., Allstadt K., Reid M.E., Collins B.D., Vallance J.W., Schilling S.P., Godt J.W., Cannon C.M., Magirl C.S., Baum R.L., Coe J.A., Schulz W.H., Bower J.B., 2015. Landslide mobility and hazards: Implications of the 2014 Oso

disaster. Earth and Planetary Science Letters, 412, 197–208. https://doi.org/10.1016/j.epsl.2014.12.020.

Jiang H., Zou Q., Zhu Y., Li Y., Zhou B., Zhou W., Yao S., Dai X., Yao H., Chen S., 2024. Deep learning prediction of rainfall-driven debris flows considering the similar critical thresholds within comparable background conditions. Environmental Modelling and Software, 179. https://doi.org/10.1016/j.envsoft.2024.106130.

Ju Y., Xu Q., Jin S., Li W., Su Y., Dong X., Guo Q., 2022. Loess Landslide Detection Using Object Detection Algorithms in Northwest China. Remote Sensing, 14. https://doi.org/10.3390/rs14051182.

Kean J.W., McCoy S.W., Tucker G.E., Staley D.M., Coe J.A., 2013. Runoff-generated debris flows: Observations and modeling of surge initiation, magnitude, and frequency. Journal of Geophysical Research: Earth Surface, 118, 2190–2207. https://doi.org/10.1002/jgrf.20148.

Keller E.A., Bean G., Best D., 2015. Fluvial geomorphology of a boulder-bed, debris-flow - Dominated channel in an active tectonic environment. Geomorphology, 243, 14–26. https://doi.org/10.1016/j.geomorph.2015.04.012.

Kirschbaum D., Stanley T., Zhou Y., 2015. Spatial and temporal analysis of a global landslide catalog. Geomorphology, 249, 4–15. https://doi.org/10.1016/j.geomorph.2015.03.016.

Kuschel E., Tolle F., Klaus V., Laa U., Prokop A., Friedt J.M., Bernard E., Zangerl C., 2024. Meteorological factors control debris slides and debris flows in a high-Arctic glacier basin (Ny-Ålesund, Svalbard). Geomorphology, 467. https://doi.org/10.1016/j.geomorph.2024.109492.

Lee S., An H., Kim M., Lee D., Lee J., 2024. Debris flows analysis through quantitative evaluation of soil depth distribution under limited data. Catena, 246. https://doi.org/10.1016/j.catena.2024.108379.

Li C.J., Hu Y.X., Fan G., Zhu Q.Y., Liu D.R., Zhou J.W., 2024. Exploring debris flow deposit morphology in river valleys: Insights from physical modeling experiments. Engineering Geology, 332, 1–15. https://doi.org/10.1016/j.enggeo.2024.107465.

Liu B., Li Y., Li G., Liu A., 2019. A spectral feature based convolutional neural network for classification of sea surface oil spill. ISPRS International Journal of Geo-Information, 8. https://doi.org/10.3390/ijgi8040160.

McKean J., Roering J., 2004. Objective landslide detection and surface morphology mapping using high-resolution airborne laser altimetry. Geomorphology, 57, 331–351. https://doi.org/10.1016/S0169-555X(03)00164-8.

Megown R.A, Webster M., Jacobs S., 1999. Using Landsat TM Imagery to Estimate LAI in a Eucalyptus Plantation, 1–13.

Meinhardt M., Fink M., Tünschel H., 2015. Landslide susceptibility analysis in central Vietnam based on an incomplete landslide inventory: Comparison of a new method to calculate weighting factors by means of bivariate statistics. Geomorphology, 234, 80–97. https://doi.org/10.1016/j.geomorph.2014.12.042.

Nava L., Bhuyan K., Meena S.R., Monserrat O., Catani F., 2022. Rapid Mapping of Landslides on SAR Data by Attention U-Net. Remote Sensing, 14, 1–15. https://doi.org/10.3390/rs14061449.

Nguyen Cong G., Nguyen Quyet C., Dang Vu K., 2024. Estimation of greenhouse gas emission due to open burning of rice straw using Sentinel data. Vietnam Journal of Earth Sciences, 46(3), 381–398. https://doi.org/10.15625/2615-9783/20716.

Nguyen H.D., Pham V.T., Nguyen Q.-H., Bui Q.-T., 2025. Soil salinity prediction using satellite-based variables and machine learning: Case study in Tra Vinh province, Mekong Delta, Vietnam. Vietnam Journal of Earth Sciences, 47, 1–19.

Nguyen Thanh H., et al., 2025. Forest cover change mapping based on Deep Neuron Network, GIS, and High-resolution Imagery. Vietnam Journal of Earth Sciences. https://doi.org/10.15625/2615-9783/22192.

Nhu V.H., Hoang N.D., Nguyen H., Ngo P.T.T., Thanh Bui T., Hoa P.V., Samui P., Tien Bui D., 2020. Effectiveness assessment of Keras based deep learning with different robust optimization algorithms for shallow landslide susceptibility mapping at tropical area. Catena, 188. https://doi.org/10.1016/j.catena.2020.104458.

Pham T.T., Dang K.B., Giang T.L., Hoang T.H.N., Le V.H., Ha H.N., 2024. Deep learning models for

monitoring landscape changes in a UNESCO Global Geopark. Journal of Environmental Management, 354, 120497. https://doi.org/10.1016/j.jenvman.2024.120497.

Pham V.T., Le H.L., Tran T.N., Nguyen Q.P., Phan T.T., Dinh T.Q., Dao M.D., Nguyen C.L., Nguyen H.C., 2023. Mechanism and numerical simulation of a rapid deep-seated landslide in Van Hoi reservoir, Vietnam. Vietnam Journal of Earth Sciences, 45, 357–373.

Pierson T., 2005. Distinguishing between debris flows and floods from field evidence in small watersheds. Water, 4.

Pouliot D., Latifovic R., Pasher J., Duffe J., 2019. Assessment of convolution neural networks for wetland mapping with landsat in the central Canadian boreal forest region. Remote Sensing, 11. https://doi.org/10.3390/rs11070772.

Pour A.B., Hashim M., 2017. Application of Landsat-8 and ALOS-2 data for structural and landslide hazard mapping in Kelantan, Malaysia, 1285–1303.

Qin X., Zhang Z., Huang C., Dehghan M., Zaiane O.R., Jagersand M., 2020. U2-Net: Going deeper with nested U-structure for salient object detection. Pattern Recognition, 106. https://doi.org/10.1016/j.patcog.2020.107404.

Ren D., 2015. Storm-triggered landslides in warmer climates. Storm-Triggered Landslides in Warmer Climates, 1–365. https://doi.org/10.1007/978-3-319-08518-0.

Sánchez-Núñez J.M., Macías J.L., Saucedo R., Zamorano J.J., Novelo D., Mendoza M.E., Torres-Hernández J.R., 2015. Geomorphology, internal structure and evolution of alluvial fans at Motozintla, Chiapas, Mexico. Geomorphology, 230, 1–12.

https://doi.org/10.1016/j.geomorph.2014.10.003.

Seale C., Redfern T., Chatfield P., Luo C., Dempsey K., 2022. Coastline detection in satellite imagery: A deep learning approach on new benchmark data. Remote Sensing of Environment, 278, 113044. https://doi.org/10.1016/j.rse.2022.113044.

Sivapriya M.S., Suresh S., 2023. ViT-DexiNet: a vision transformer-based edge detection operator for small object detection in SAR images. International Journal of Remote Sensing, 44, 7057–7084. https://doi.org/10.1080/01431161.2023.2277167.

Stoian A., Poulain V., Inglada J., Poughon V., Derksen D., 2019. Land cover maps production with high resolution satellite image time series and convolutional neural networks: Adaptations and limits for operational systems. Remote Sensing, 11, 1–26. https://doi.org/10.3390/rs11171986.

Studer M., Falbel M.D., 2019. Keras Package Manual. Su B., Li Y., Han Z., Ma Y., Wang W., Ruan B., Guo W., Xie W., Tan S., 2024. Topography-based and vectorized algorithm for extracting physical quantities in 3D-SPH form and its application in debris-flow entrainment modeling. Engineering Geology, 340. https://doi.org/10.1016/j.enggeo.2024.107693.

Thao V.B., Huong N.T.T., 2022. Assessing the morphological characteristics of stream basins on the formation of flash floods in the mountainous region of Northern Vietnam. Journal of Irrigation Science and Technology, 70, 1–16.

Tram T., Bac K., Linh T., Huyen T., Hoang N., Le V.H., 2024. Deep learning models for monitoring landscape changes in a UNESCO Global Geopark. Journal of Environmental Management, 354, 120497. https://doi.org/10.1016/j.jenvman.2024.120497.

Tran Anh T., Pham Viet H., Tran Thi T., Nguyen Thi Anh N., Nguyen Van D., Pham Tuan H., Tran Van P., 2024. Landslide susceptibility in Phuoc Son, Quang Nam: A deep learning approach. Vietnam Journal of Earth Sciences, 47(1), 39–57. https://doi.org/10.15625/2615-9783/21658.

Tran T.H., 2013. Relationship between geomorphology and landslide in Lao Cai province. VNU Journal of Science, 3, 35–44.

Van Thang N., Sato G., Wakai A., Hung H.V., Ducmanh N., Kimura T., Yamasaki T., Tosa S., Hayashi K., Watanabe A., Ozaki T., Asai N., Kitamura N., 2021. Landslide investigation results in SAPA town, Lao CAI province, Vietnam in December 2019. Journal of Disaster Research, 16, 547–555. https://doi.org/10.20965/JDR.2021.P0547.

Varma Byrraju S., 2019. Scholar Commons Scholar Commons Landslide Detection Using Remote

Sensing Methods A Review of Landslide Detection Using Remote Sensing Methods A Review of Current Techniques Current Techniques.

Vu B.T., Nguyen T.T.H., 2023. Impact mechanisms and morphological characteristics of Nam Pam debris flow - flash flood catchment. Ministry of Science and Technology, Vietnam, 65, 58–66. https://doi.org/10.31276/vjst.65(6).58-66.

Wang L., Yang Y., Min R., Chakradhar S., 2017. Accelerating Deep Neural Network Training with Inconsistent Stochastic Gradient Descent. Computer Science, Machine Learning,Cornell University, 3, 12.

Wen S., Yuan Y., Chen J., 2023. A Vision Detection Scheme Based on Deep Learning in a Waste Plastics Sorting System. Applied Sciences (Switzerland), 13. https://doi.org/10.3390/app13074634.

Yang H., Liu J., Sun H., You Y., Zhao W., Yang D., 2024. Evolution characteristics of post-fire debris flow in Xiangjiao gully, Muli County. Catena, 246. https://doi.org/10.1016/j.catena.2024.108353.

Yang S., Mei G., Zhang Y., 2024. Susceptibility analysis of glacier debris flow by investigating glacier changes based on remote sensing imagery and deep learning: A case study. Natural Hazards Research, 4, 539–549. https://doi.org/10.1016/j.nhres.2023.12.013.

Yasir M., Liu S., Pirasteh S., Xu M., Sheng H., Wan J., de Figueiredo F.A.P., Aguilar F.J., Li J., 2024a. YOLOShipTracker: Tracking ships in SAR images using lightweight YOLOv8. International Journal of Applied Earth Observation and Geoinformation, 134, 104137. https://doi.org/10.1016/j.jag.2024.104137.

Yasir M., Shanwei L., Mingming X., Jianhua W., Nazir S., Islam Q.U., Dang K.B., 2024b. SwinYOLOv7: Robust ship detection in complex synthetic aperture radar images. Applied Soft Computing, 160, 111704. https://doi.org/10.1016/j.asoc.2024.111704.

Yousefi S., Imaizumi F., Takayama S., 2025. Spatial distribution and transport characteristics of debris flow sediment using high resolution UAV images in the Ohya debris flow fan. Geomorphology, 469, 109533. https://doi.org/10.1016/j.geomorph.2024.109533.

Zhang J., Cheng H., Wu S., Wu G., Tuo R., Liu W., Xinglong Feng, Li Z., 2024. Risk analysis of underground debris flows in mines based on a coupled weighted Bayesian network. International Journal of Disaster Risk Reduction, 114. https://doi.org/10.1016/j.ijdrr.2024.104922.

Zhang L., Zhang J., Ming Z., Li H., Chen R., Jia Y., 2024. Effects of changing spatial scale on debris-flow hazard assessment: A case study in the Dadu River basin, China. Science of the Total Environment, 954. https://doi.org/10.1016/j.scitotenv.2024.176482.

Zhang P., Liu X., Shu H., 2023. Hazard assessment of debris flow by using FLO-2D and hazard matrix: a case study of Qingshui Gully in the southern Gansu Province, China. Desalination and Water Treatment, 315, 650–662. https://doi.org/10.5004/dwt.2023.30108.

Zhou W., Zhou Y., Liu R., Yin H., Nie H., 2025. Predictive modeling of river blockage severity from debris flows: Integrating statistical and machine learning approaches with insights from Sichuan Province, China. Catena, 248. https://doi.org/10.1016/j.catena.2024.108576.